



OPEN Demonstration of a novel method to explore osteon tilt in the human femoral cortex

Suzanna Michener¹✉, Nadine C. Schuurman², David Swanlund² & Lynne S. Bell¹

Osteon tilt, defined as the combination of an osteon's vertical angle and horizontal orientation, remains poorly characterized due to technical limitations in large-scale 3D bone microarchitecture analysis. This study developed a methodology combining traditional serial sectioning using circularly polarized light microscopy with Geographic Information Systems (GIS) to visualize and quantify osteon tilt across the entire femoral cortex. Spatial variation of osteon tilt was analyzed using 1219 osteons across 8 octants and 3 circumferential rings. Vertical osteon angle varied regionally, with acute angles in the anterolateral region and obtuse angles in the posterior region. Osteons demonstrated a general posterior inclination with opposite orientations on the medial and lateral cortices. Vertical angle positively correlated with osteon volume, with the strongest correlation found in the anterior and lateral regions. A paired sample t-test showed no significant difference between serial sections, confirming the preservation of sectional alignment. Osteon tilt patterns may reflect the femur's complex loading environment: smaller, acutely angled osteons predominate in tension-bearing regions, while larger, obtusely angled osteons occur in compression-bearing regions. This GIS-based method enables a quantitative, comprehensive assessment of osteon morphology and provides insights into bone's adaptive remodeling response to biomechanical forces.

Keywords Bone, Histology, Osteons, Osteon tilt, Biomechanics, GIS

The study of osteon systems traverses biological fields with applications in medical pathology¹, biomechanics^{2–4}, and forensic science⁵, among others. Three-dimensional examination of secondary osteons, the observable structural unit of bone remodeling, has conventionally been understood through two-dimensional observation^{6,7}. Improved methodologies for the three-dimensional investigation of cortical bone microarchitecture regularly suggest a greater organizational complexity than was formerly considered^{8,9}. Ex vivo imaging modalities, including micro-computed tomography and synchrotron radiation micro-CT improve 3D visualization but share a limitation: higher resolution reduces the field of view^{6,10}. Incorporating Geographic Information Systems (GIS) science into bone histomorphometry^{11–13} can circumvent this issue by three-dimensionally relating and visualizing osteons, and quantifying structural characteristics, across the entire cortex and through multiple serial transverse sections¹⁴. A GIS-based protocol enables exploration of osteon tilt.

Bone remodeling

Bone adapts to dynamic strains and many of its properties are dependent on loading stresses from weight-bearing activities^{15–17}. Such forces contribute to bone remodeling^{18–20}, a continuous maintenance process that repairs skeletal damage, replaces dead or hypermineralized bone, and maintains chemical homeostasis^{4,21–24}. Remodeling occurs through the coordinated action of osteoclasts and osteoblasts in a six-stage cycle: activation by osteocytes, resorption by osteoclasts, reversal from bone resorption, formation by osteoblasts, mineralization of the formed osteoid, and termination or quiescence until future activation^{20,23,25–27}. Bone remodeling may be non-targeted, which occurs as a response to systemic changes unrelated to microdamage, functioning as a form of mineral homeostasis^{18–20,28}. Conversely, local microdamage from biomechanical strain in the bone matrix initiates targeted remodeling^{29–35}. Osteocytes sense changes within the lacunar-canalicular network and respond to these localized forces³⁶. Through the process of mechanotransduction^{24,29,37} osteocytes convert physical forces into biochemical pathways to direct targeted remodeling^{38–42}. The structural outcome of this process is a cutting cone^{43,44}, which directs the final path of the secondary osteon^{6,21} (Fig. 1), and other properties, including its volume, orientation, shape, and size. Secondary osteons are typically circular to elliptical in cross section⁴⁵,

¹Centre for Forensic Research, School of Criminology, Simon Fraser University, 8888 University Drive, Burnaby V5A 1S6, Canada. ²Department of Geography, Simon Fraser University, 8888 University Drive, Burnaby V5A 1S6, Canada. ✉email: smichene@sfu.ca

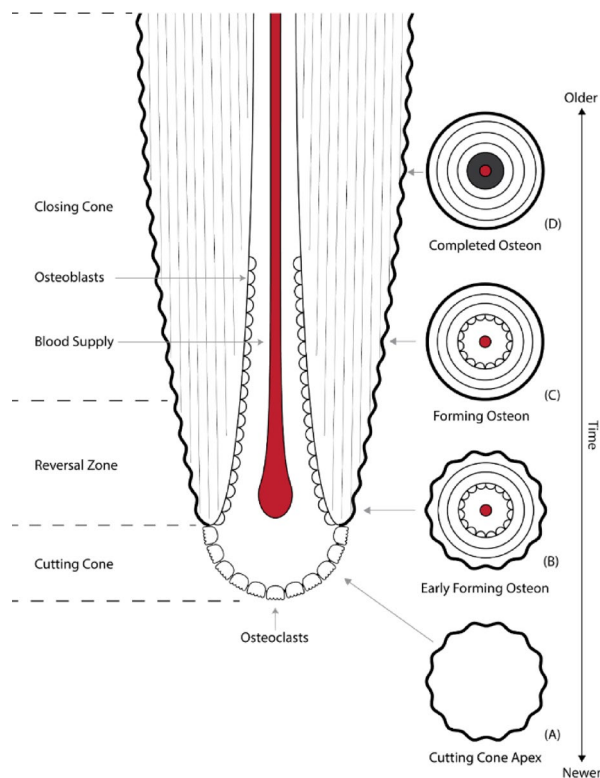


Fig. 1. Left: Schematic of a forming osteon showing the conical shape of the cutting cone. Osteoclasts dissolve the bone matrix, creating the cutting cone and the subsequent osteon properties. Osteoblasts follow and infill the cone. Right: Schematics of transverse sections at time-related remodeling locations. (a) Cutting cone apex, (b) Early forming osteon, (c) Forming osteon, (d) Completed osteon.

conical to tubular in structure^{14,17}, range from 100 to 350 microns in diameter⁴³, and may be up to 10 mm in length⁶ but are often much shorter, with a reported mean of 2.7 mm⁴⁶, after which point they begin branching⁴⁷. Osteons grow approximately parallel to the long axis of the bone, but their size and shape vary longitudinally, which relates to their degree of network connectivity⁴⁵. Although osteon systems are typically depicted as a tidy nest of cylinders, contemporary visualization demonstrates that osteons can branch, overlap, bud, end blindly, connect transversely, infill incompletely, and change direction, simultaneously tunneling proximally and distally^{9,14,48–51}. Because biomechanical forces initiate targeted remodeling, they have been implicated in osteon structural complexity^{21,52}, as well as osteon size^{50,52}, osteon circularity⁵⁰, osteon population density^{53,54}, Haversian canal diameter⁵³, osteon morphotype⁵⁵, and the orientation of collagen fibrils, which comprise the concentric lamellae that surround the Haversian canal^{55–57}.

Osteon tilt

Osteon tilt, a three-dimensional measurement comprised of the osteon's vertical trajectory and horizontal orientation, may also be related to biomechanical forces^{47,48,58–61}, as cutting cone trajectories follow the direction of prevalent local stresses^{62,63}. Early work on tilt describes an oblique orientation with osteon systems organized in two hemi-spirals of opposite directions in the medial and lateral walls of the diaphysis, sharply separated on the anterior and posterior aspects⁶⁴. Cohen and Harris⁴⁸ noted helical clockwise osteon direction around the diaphyseal circumference from its periosteal to endosteal surfaces in canine femora. Human femoral diaphyses exhibit similar spiral patterns, with osteons grouped in two helical anti-rotary systems of opposite oblique directions, situated contralaterally with distinct boundaries between the medial and lateral fields^{58–65}. Some studies did not identify this oblique orientation^{47,49,59,66}, possibly due to sampling strategy, species selection, individual differences, visualization methods, and the general lack of research in this area.

The helical anisotropy commonly seen^{48,58,60,64,65} relates to the dominant osteon direction and corresponding bending, compression, and torsional loading moments^{48,53,60,65,67}. The most comprehensive study noted that osteon systems within long bones were consistently arranged obliquely in two helices separated by sharp boundaries, a pattern explained by dominant loading modes⁶⁰. Specific to the right femur, the right-spinning helical orientation on the lateral wall and the left-spinning orientation on the medial wall corresponds with dominant principal stress directions from a combined left-spinning torque moment and a dominant bending moment in the frontal plane. Osteon orientation has also been studied in the peritrochanteric femur, where they run parallel to the longitudinal axis of the femoral neck, corresponding to loading in that region¹. Osteon tilt has also been analyzed in animal long bones, with bending and torque moments impacting osteon orientation in sheep tibiae⁶¹ and shear strains contributing to oblique osteon systems in deer calcanei⁶⁷.

Fewer studies explore the angle of osteon tilt than the patterning of osteon orientation. In their comprehensive study, Heřt et al.⁶⁰ calculated osteon longitudinal angle ranges from 0° to 15° in human limb long bone, and provided two mean vertical angles for femoral osteons: 8.1° on the lateral half and 10.3° on the medial half. Osteons in canine femora are obliquely oriented between 11° and 17°⁴⁸, and within sheep tibiae samples osteons are oriented at 11.5° in the cranial cortex, which is attributed to tensile loading, and 9.5° in the caudal cortex, due to compressive forces⁶¹. 3D volume electron microscopy and deep-learning segmentation methods corroborate this helicoid trajectory around sheep's femoral shaft axis at a pitch of 5–15°⁶⁸. As with orientation, osteon vertical angle has been attributed to biomechanical loading^{48,58,60,61}.

Three-Dimensional visualization

Technical limitations may explain why osteon tilt is under-researched. Most 3D histological structures were interpreted from 2D transverse ground sections, requiring idealization and assumption^{6,7}. Serial sectioning adds a vertical dimension but large-scale 3D information is limited because only portions of bone can be analyzed, so may not be generalizable outside the region of interest⁶⁹, and because techniques are destructive and not yet automated⁷⁰. The capabilities of x-ray micro-CT and synchrotron radiation micro-CT eliminate the need for extrapolation as 3D structures are directly observable and measurable, but are limited by a decreased field of view when increasing resolution, which also increases the radiation dose, restricting the potential for *in vivo* studies^{6,70}. High Resolution peripheral Quantitative CT can visualize human cortical porosity *in vivo*⁷² and focused ion beam-scanning electron microscopy can examine osteons to the nanometer⁷³.

Incorporating GIS software into traditional histological protocols can bridge the 2D-3D gap. GIS is considered a 2.5D software environment as it allows *z*-plane values but lacks the ability to fully model in 3D^{74,75}. The 2.5D nature permits enhanced visual and spatial data analysis and only lacks the ability to infer complex 3D structures^{74,75}. For visualizing and quantifying biological structures, GIS offers an understanding of spatial data and activity through mathematical modeling¹². Combining serial sectioning with a GIS protocol duplicates benefits of micro-CT and synchrotron radiation micro-CT imaging, while mitigating some challenges. There are no field-of-view or resolution limitations, and GIS software is designed to handle large images and datasets^{76,77}. All microstructural features across an entire transverse section can be visualized and analyzed⁷⁸ through connected serial layers forming extrapolated 3D images. Spatial data can be identified, measured, and compared between 2D layers, or on a combined 3D composite, where rarely explored microarchitectural variables, including osteon volume or tilt, can be studied at a large scale^{13,14}. Mapping spatial relationships in 3D also allows for network modeling to understand temporal progression, meaning that GIS software can infer a fourth dimension of time^{12,27}. And although challenges exist, such as choosing an appropriate coordinate system, choosing appropriate reference points, measuring distances, and regionalization¹², numerous studies^{11,13,14,54,79–82} demonstrate the viability of GIS applications to 3D biological examination.

The objective of this research study is to establish a method to visualize and quantify the spatial patterning of osteon tilt around the femoral cortex, through a comparative quantitative analysis of the vertical angle and the horizontal orientation of osteons. This is achieved by using a GIS-based methodological protocol designed for three-dimensional osteon visualization. Improved conceptualization and quantification of osteon tilt patterns may yield insight into how biomechanical inputs affect osteon remodeling properties and increase understanding of the factors that govern bone microstructural development.

Methods

Ethics approval for this project was granted by Simon Fraser University's Office of Research Ethics (study no. 2018s0137). All methods were carried out in accordance with relevant guidelines and regulations.

Sample Preparation

This research employed a GIS-based method developed by Michener et al.¹⁴ to quantify osteon volume in three-dimensions (Fig. 2). To develop the method, a transverse block was cut from the right femoral midshaft of an adult human femur of unknown origin obtained from a teaching collection. Before sectioning, four vertical orienting grooves were cut into the outer cortex of the bone block to mimic compass points and to aid in georeferencing, or aligning, overlapping spatial data (Fig. 3). Three thin serial transverse sections were cut from the bone block using a Leica SP microtome (Leica Biosystems). The superior (S) section was 61+/-6 µm thick, the middle (M) section was 70+/-4 µm thick, and the inferior (I) section was 65+/-5 µm thick. Each section was separated by 300 µm due to the thickness of the blade, so when compiled, the *z*-axis of the three sections measured approximately 810 µm, with 600 µm missing from the viewable area.

The serial sections were mounted on slides and photo-montaged using circularly polarized light at an overall magnification of 25x with a Zeiss Axio Scope A.1 (Zeiss) and a Zeiss 105 color microscope camera (Zeiss). Each micrograph was processed using Zeiss Zen Lite Software (Zeiss) and then exported and composited using Microsoft Image Composite Editor (Microsoft). Composites were imported into Adobe Photoshop CS6 (Adobe) for minor adjustments to clarity and contrast. Final images were exported as a 2GB, 1 gigapixel TIFF (tagged image file format). These transverse composites were imported as raster layers into ArcGIS for methodological development.

GIS processing

The volumetric method was originally developed using ArcGIS 10.3, but all steps can be performed using ArcGIS Pro 3.1, which was used in the current study to analyze osteon tilt. GIS tools were selected because they can overlay, connect, and calculate various parameters of spatially referenced layers more readily and accurately than visualization software, which does not account for the movement and structural variation that exists in osteon systems. Once imported, the TIFF micrographs were projected at an appropriate coordinate system.

GIS-BASED VOLUMETRIC METHOD TO CALCULATE OSTEON TILT

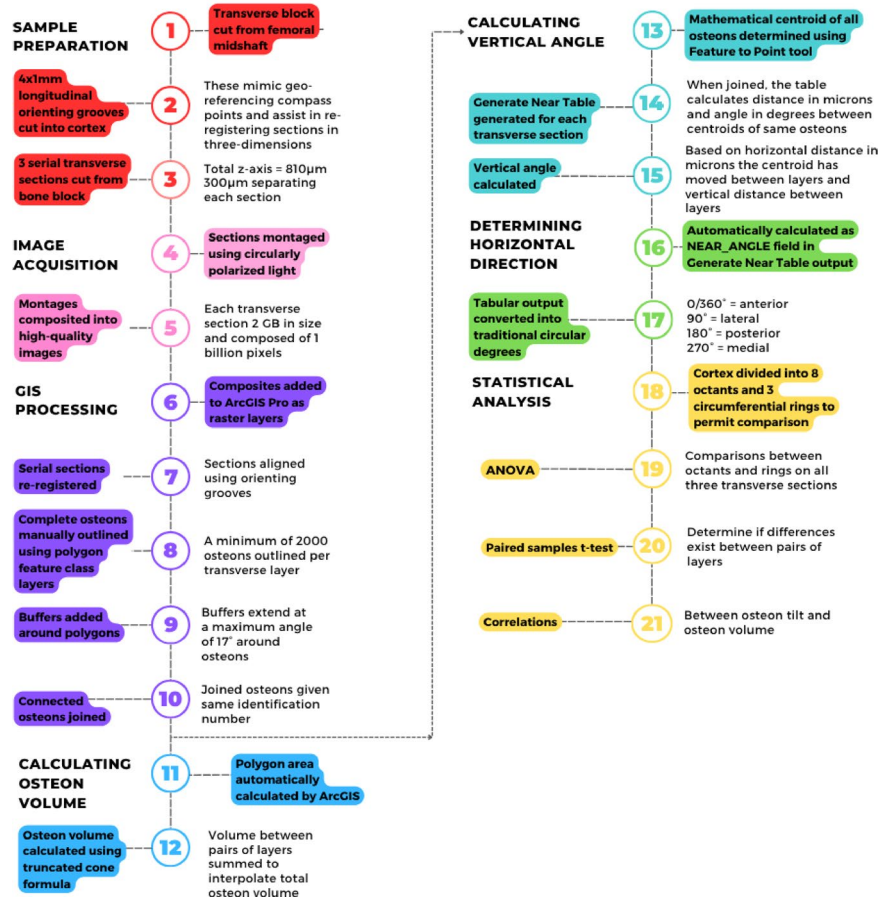


Fig. 2. Flowchart presenting the steps to the volumetric method as outlined in Michener et al. (2020) and the steps to the current method of calculating osteon tilt.

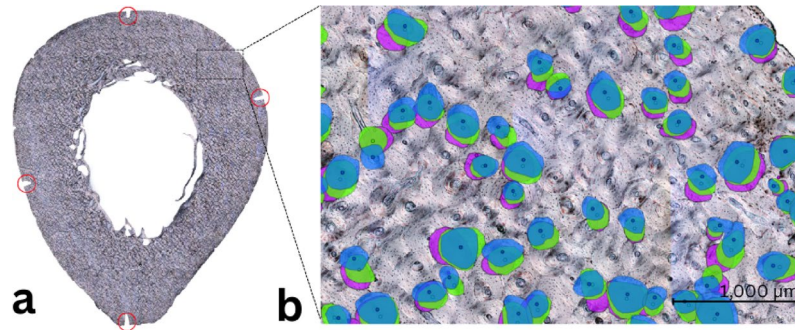


Fig. 3. **A:** ArcGIS Pro export of the composite of the superior femoral transverse section. Orienting grooves used for re-alignment of serial sections are circled in red. The orienting grooves were cut into the bone before sectioning and the three serial sections were overlaid and aligned using these grooves. **B:** ArcGIS Pro export of a close-up of the three layers polygons overlaid atop a composite micrograph of the superior transverse section. Blue osteons represent the superior layer, green osteons represent the middle layer, purple osteons represent the inferior layer. Composite micrographs of the middle and inferior sections are not shown for clarity. Mathematical centroids used to calculate osteon tilt are shown within the polygons.

As GIS software is not intended for use on the microscopic scale, most coordinate systems are in meters; thus, distance was converted into microns for accurate calculations. The orienting grooves in exterior cortex served as georeferenced data points, mirroring fixed locations on the surface of the Earth. Using the grooves, the three serial sections were overlaid and aligned using control points to permit tracking individual osteons through the sections (Fig. 3).

The method was originally developed to calculate osteon volume¹⁴, so osteons had to be connected between the three transverse sections. A polygon feature class layer was added to each transverse section. A minimum of 2000 intact secondary osteons per transverse section, identified as having an intact Haversian canal and bounded by a reversal line⁸³, were manually outlined as polygons by one researcher (SM) and verified by another (LSB) (Fig. 3). Polygons that represented the same osteon across the three transverse sections were connected using buffers, a unique feature of ArcGIS's proximity toolset. Buffers determine where a zone of measurement extends from a particular map feature to a specified distance⁸⁴. The buffers accommodated the tilted longitudinal trajectory of osteons, which was established at a maximum angle of 17° off the vertical z-axis plane, based on a reference by Burr & Akkus³⁵. Subsequent investigation revealed this angle was derived from Cohen and Harris's⁴⁸ and Lanyon and Bourn's⁶¹ research on dog femora and sheep tibiae, respectively. More recent and appropriate (i.e. based on humans) research discussed above^{60,65} indicates that osteons are oriented at a different range of angles in humans, and that this orientation also differs based on the skeletal element and location within the skeletal element and the contributing biomechanical forces. However, the research on human femora indicates that the 17° buffer should encompass most osteon trajectories, thus was suitable for methodological development and did not require adjustment for methodological refinement. Using this angle, and a vertical distance of 370 µm (the distance between the sections plus the thickness of the section), Pythagorean geometry calculated the buffer distance around each polygon as 116 µm. Using the First Law of Geography⁸⁵, which states that "everything is related to everything else, but near things are more related than distant things" (236), buffers help to identify which osteons in a cluster may be connected to osteons from a separate layer, based on their nearness to each other and similar properties. Osteons in close proximity are statistically more likely to share characteristics than those farther away, such as a similar size or shape, enabling osteon identification and connection between sections.

Calculating osteon volume

Calculating osteon volume requires the measurement of osteon area. ArcGIS automatically calculates the area of the polygon features. Osteons form via a cutting cone (Fig. 1), but because the osteons identified using this method extend beyond the viewable area, volume was calculated using a truncated cone geometric function:

$$V = \pi \times h \times (R^2 + Rr + r^2)/3$$

h = z-axis distance between sections (370µm)
 R = radius of the upper osteon
 r = radius of the lower osteon

The volume of the truncated cone was calculated for the superior and middle transverse sections, and the middle and inferior sections; the calculations were summed to estimate the volume of the viewable portion of the osteon, measuring approximately 810 µm in length.

Osteon tilt

Calculating osteon tilt begins with the use of buffers to identify, label, and re-register connected osteons between the three serial transverse sections (Fig. 2). The GIS-based method was adapted to explore osteon tilt, which was evaluated using two variables: osteon angle and osteon orientation (Fig. 4). Osteon angle measures the z-plane off-axis inclination, or the vertical trajectory the osteon takes. Osteon orientation assesses which anatomical plane osteons are oriented towards by evaluating the direction osteons travel on the x-y plane, as determined by which direction the osteon moves based on the changing position of its centroid between layers. Together, these variables measure tilt, which is the off-axis inclination and orientation of the entire osteon. Osteon angle is measured in degrees of change from straight vertical, so 0° indicates that the osteon is perfectly vertical, and (for example) 10° indicates a slight tilt to the osteon. To permit statistical comparison, osteon orientation is represented in circular degrees, where 0°/360° indicates that between serial sections the osteon's centroid moves towards the anterior of the bone, and 180° means the osteon travels posteriorly. As this was developed using a right femur, 90° indicates the osteon moves laterally between sections and 270° indicates the osteon travels towards the medial between sections (Fig. 5).

Calculating osteon vertical angle

The vertical angle of connected osteons was calculated using two features unique to ArcGIS: centroid determination and the proximity toolset⁸⁶. The centroid, or mathematical center, of each osteon from each vector layer was determined using the *Feature to Point* tool (Fig. 3). Centroids were used rather than mapping the Haversian canals because centroid determination is an automatic function and because tilt is measuring the inclination of the cutting cone, which includes the Haversian canal. The *Generate Near Table* function within the proximity toolset determined the distance in microns and the angle in degrees between the centroid of an osteon on one layer and the centroid from the same osteon on the other layers. This function supports finding more than one nearest feature⁸⁷ and will rank all nearby features in order of nearness, an asset when connecting dynamic and densely clustered structures like osteons. Despite being commonly represented as simple stacked cylinders, osteons instead branch, bud, and change direction⁹. Therefore, a single osteon may not be in the same location in

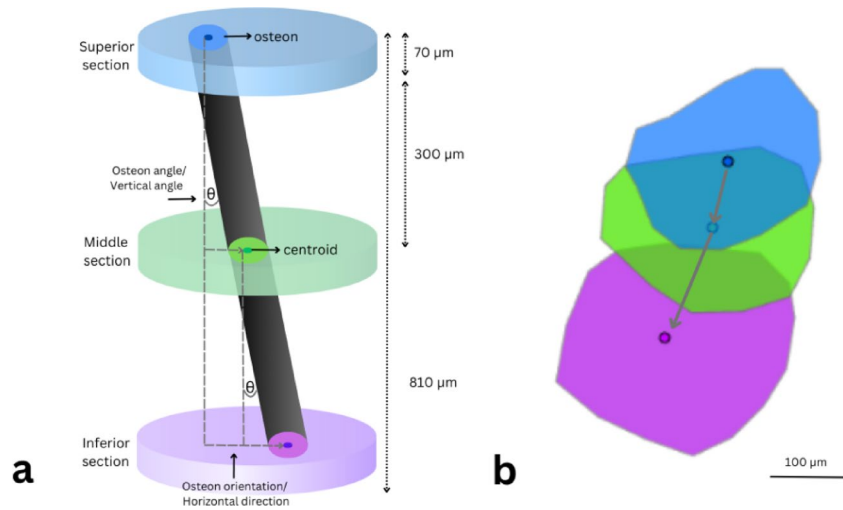


Fig. 4. **A:** Schematic representing the measurements for calculating osteon tilt. Osteon angle measures the vertical off-axis tilt of the osteon as it traverses longitudinally through bone on the *z*-plane. Osteon angle was measured between the superior and middle layers, the middle and inferior layers, and the superior and inferior layers. Osteon orientation measures the horizontal direction that the osteon travels on the *x-y* plane. The angle in circular degrees represents the anatomical direction the osteon is moving towards as it travels longitudinally. Although the osteon is represented as a cylinder in the schematic, osteon volume was calculated using the truncated cone formula because of their formation via cutting cone and because osteons extend beyond the viewable area. **B:** ArcGIS Pro export of a sample of polygons that outline osteons in the lateral cortex. Blue polygons represent osteons in the superior layer, green polygons represent osteons in the middle layer, and purple polygons represent osteons in the inferior layer. Arrows between the centroids show the general path of the osteons as they travel longitudinally through the bone, representing osteon orientation.

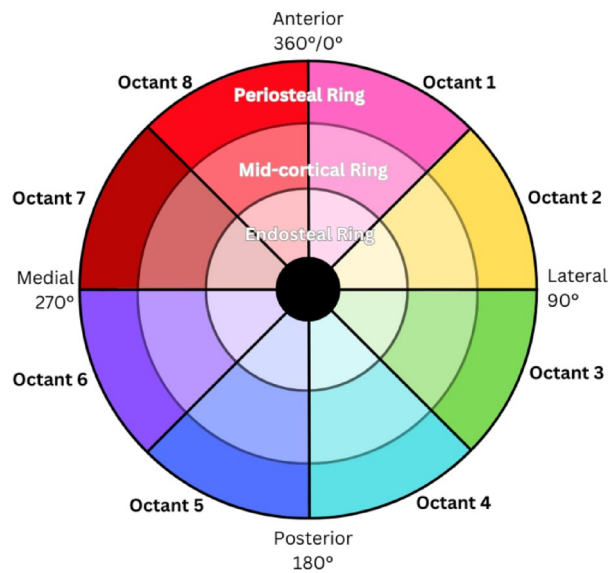


Fig. 5. The octant and circumferential ring system employed.

sequential layers, and osteons that appear to directly overlap in sequential layers may not be the same osteon. By measuring nearest neighbor distances, the osteons can be ranked (NEAR_RANK) based on their closeness to all other osteons in the selected layer. Osteons from the sequential layers that share the same identification number were ordered to ensure that each was either the first or second closest osteon to the corresponding osteon in each layer. Those outside this ranking were manually reviewed and the correct measurements were obtained. The nearest neighbor tabular output automatically calculates the horizontal distance (HD) between the nearest osteon centroids. This measures how far horizontally, in microns, the osteon’s centroid has moved between two sequential layers. The distance between sections, which is due to blade thickness in the serial sectioning process, is 300 μm and represents the vertical distance (VD). The vertical angle (θ) was calculated as:

$$\sin(\theta) = HD/\sqrt{HD^2 + VD^2}$$

HD = horizontal distance

VD = vertical distance

Calculating osteon horizontal direction

The *Generate Near Table* function within the proximity toolset automatically calculates the horizontal direction (NEAR_ANGLE) of osteon orientation on the *x-y* plane as an angle from the *x*-axis. The values were converted to positive numbers and transformed into circular degrees aligned with anatomical structure, where 0°/360° indicates that the osteon moves towards the anterior as it travels between serial sections, 90° represents a lateral direction, 180° represents a posterior direction, and 270° represents a medial direction (Fig. 5).

Dividing the cortex

To explore the spatial variation of osteon tilt, the femoral cortex was subdivided into eight octants and three circumferential rings; however, an advantage of this method is that it permits any sort of spatial comparison of the cortex (Fig. 5). Octants were created by determining the mathematical center of the entire cortex using the *Feature to Point* tool. Four lines bisecting the centroid and separated by 45° created an eight-pronged spoke that divided the cortical area into halves, quadrants, and octants, permitting comparison between these areas of interest. The circumferential rings were created by adding two polygon features: the first to overlay the entire cortex, and the second to overlay the medullary cavity of the bone. The medullary cavity polygon was subtracted from the complete cortical polygon and the resulting area was divided into equal thirds. Polygon features were created for each third, dividing the cortex into periosteal (exterior), mid-cortical (middle), and endosteal (interior) cortical regions. The sparse research on osteon tilt suggests that regional variation exists, so the octant division was necessary to compare results of this study to previous research and to provide a more detailed analysis of regional variation. Octants provide more data on spatial variation than cortical halves or quadrants, but data can easily be combined into these traditional divisions. Earlier research either did not find or did not examine circumferential regional differences. However, circumferential regional variation has been explored in research on the spatial patterning of osteon population density⁵⁴ and collagen fibril orientation⁸⁸. Collagen fibers can be oriented transversely and longitudinally and are structured to withstand compressive and tensile strains, respectively^{89,90}, and these strains vary in different quadrants and circumferential rings of the femoral midshaft^{55,88,91}. The same system of division was utilized in the current research to explore if osteon tilt may be impacted by similar biomechanical properties as collagen fibrils.

Octant and circumferential ring statistical comparison

ANOVA comparisons assessed the differences between the mean vertical osteon angle and the mean horizontal osteon orientation. Comparisons were made between the superior and middle (SM) and middle and inferior (MI) layers for each octant and circumferential ring. Octants were compared with each other, and circumferential rings were compared with each other to evaluate regional differences. The regional comparisons were repeated between the superior and inferior (SI) layers to see if measurements of osteon tilt were consistent across a greater distance, in an examination of graded depth. Tukey's HSD post-hoc test determined the specific differences between the mean osteon angle and mean osteon orientation between octants and circumferential rings.

Statistical comparisons between serial layers

A paired sample t-test was performed to determine if there were significant differences between the two pairs of layers (SM and MI). These pairs of layers consist of the same osteons, so no differences and a strong correlation would demonstrate appropriate alignment of the transverse sections and support validity of the GIS-based protocol.

Correlation between osteon volume and osteon vertical angle

Lastly, correlations were run to ascertain if there was a relationship between average osteon vertical angle and average osteon volume, per octant. The regional variation of osteon volume is likely influenced by biomechanical inputs¹⁴, as damage and subsequent remodeling of these forces impact osteon area, a variable necessary to calculate osteon volume^{50,52}. Correlation between osteon volume and osteon vertical angle could indicate similar biomechanical influences on these microarchitectural variables.

All statistical analyses were conducted using SPSS v.29 and applied a critical alpha of 0.05.

Results

Overall descriptives

This research sought to utilize a GIS-based method to measure osteon tilt. Comparisons were performed between 24 regions (eight octants and three circumferential rings) across three serial transverse sections to assess the spatial variation of osteon tilt. From 2239 outlined osteons from the superior layer, 2275 osteons from the middle layer, and 2333 osteons from the inferior layer, 1219 (approximately half) of the osteons were connected between all three transverse sections. An osteon may not connect between layers if it becomes fragmentary, if it branches and becomes two, if it has not completed its formation, if it terminated in the space between sections, or if it is clustered and cannot be accurately identified as a single connected osteon.

Means were obtained and compared for osteon angles and osteon orientation for the three sets of layers (Table 1). Osteon vertical angle averages and ranges were consistent between the two shorter spans, and consistent with those from the longer span. The SM layer mean was 11.9°, with a standard deviation of 3.9, and angles ranged from 2.1° to 23.8°. The MI layer mean was 11.9°, with a standard deviation of 4.0, and angles ranged

	n	Superior-middle layer 300 μm		Middle-inferior layer 300 μm		Superior-inferior layer 810 μm		
		Osteon Angle	Osteon Orientation	Osteon Angle	Osteon Orientation	Osteon Angle	Osteon Orientation	Osteon Volume
		$x \pm \text{SD}$	$x \pm \text{SD}$	$x \pm \text{SD}$	$x \pm \text{SD}$	$x \pm \text{SD}$	$x \pm \text{SD}$	$x \pm \text{SD}$
All osteons	1219	12.0° \pm 3.9	152.0° \pm 84.8	11.9° \pm 4.0	151.7° \pm 84.1	11.1° \pm 3.8	151.9° \pm 84.2	33.5 \pm 14.2
Octant 1	212	10.6° \pm 0.2	61.4° \pm 1.9	10.6° \pm 0.2	58.8° \pm 2.0	9.6° \pm 0.2	61.2° \pm 1.9	31.9 \pm 13.3
Octant 2	240	12.2° \pm 0.3	78.8° \pm 1.8	12.1° \pm 0.3	80.2° \pm 1.6	11.5° \pm 0.3	79.7° \pm 1.8	25.6 \pm 11.8
Octant 3	128	13.3° \pm 0.3	121.7° \pm 2.5	13.1° \pm 0.3	121.9° \pm 2.4	11.7° \pm 0.3	121.9° \pm 2.5	34.1 \pm 12.5
Octant 4	128	13.6° \pm 0.3	167.8° \pm 2.7	13.4° \pm 0.3	170.4° \pm 2.7	12.4° \pm 0.3	169.4° \pm 2.8	40.2 \pm 15.9
Octant 5	141	12.5° \pm 0.3	180.1° \pm 3.0	12.3° \pm 0.3	178.8° \pm 2.9	11.5° \pm 0.3	177.6° \pm 2.9	34.6 \pm 13.9
Octant 6	122	13.0° \pm 0.3	191.7° \pm 3.9	13.0° \pm 0.3	191.0° \pm 3.6	12.1° \pm 0.3	190.9° \pm 4.1	35.0 \pm 12.6
Octant 7	128	11.0° \pm 0.4	237.6° \pm 4.1	11.2° \pm 0.3	237.8° \pm 4.0	10.8° \pm 0.4	237.2° \pm 3.8	36.6 \pm 13.8
Octant 8	120	10.4° \pm 0.3	309.1° \pm 2.9	10.5° \pm 0.3	306.5° \pm 3.1	10.0° \pm 0.3	308.5° \pm 3.0	38.2 \pm 15.0
Periosteal ring	604	11.5° \pm 0.2	153.0° \pm 3.8	11.4° \pm 0.2	153.8° \pm 3.7	10.8° \pm 0.2	154.0° \pm 3.7	
Mid-cortical ring	436	11.9° \pm 0.2	151.6° \pm 3.9	12.1° \pm 0.2	150.0° \pm 3.9	11.0° \pm 0.2	150.2° \pm 3.9	
Endosteal ring	179	13.6° \pm 0.3	149.5° \pm 4.8	13.3° \pm 0.3	148.5° \pm 4.7	12.3° \pm 0.2	148.6° \pm 4.8	
Min. value	1219	2.1°	0.5°	2.5°	5.4°	1.6°	2.6°	
Max. value	1219	23.8°	359.8°	23.8°	355.4°	24.8°	358.4°	

Table 1. Descriptive statistics (number (n), means and standard deviation ($x \pm \text{SD}$), minimum angle, and maximum angle) for osteon vertical angle and osteon horizontal direction for each set of transverse section by layer, octant, and circumferential ring. Osteon angle measures the off-axis inclination on the z -plane, or the vertical trajectory the osteon travels as it descends longitudinally towards the distal end of the femur. Horizontal osteon orientation is the direction an osteon travels on the x - y plane, or the inclination the osteon points towards on the horizontal plane, where 0°/360° represents an anterior orientation, 90° represents a lateral orientation, 180° represents a posterior orientation, and 270° represents a medial orientation. Osteon volume (mm^3) is only presented for the superior-inferior layer as it is a sum of the osteon volume for the two shorter layers.

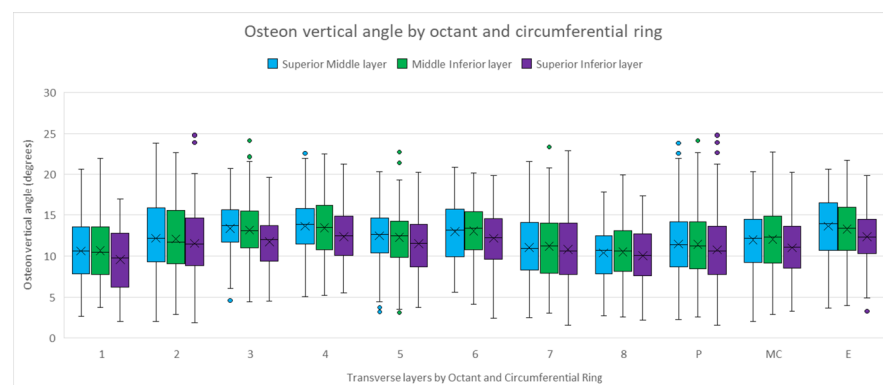


Fig. 6. Box plot showing the mean vertical angle of osteons across the octants and circumferential rings. Blue represents the connected osteons between the superior and middle layers, a distance of approximately 300 μm . Green represents the connected osteons between the middle and inferior layers, a distance of approximately 300 μm . Purple encompasses the entire viewable osteon between the superior and inferior layers, a distance of approximately 810 μm .

between 2.5° to 23.8°. The SI layer mean was 11.1° with a standard deviation of 3.8, and angles ranged from 1.6° to 24.8° (Fig. 6). The average osteon horizontal direction for the superior, middle, and inferior transverse sections was 152.0°, 151.6°, and 151.8°, with a standard deviation of 84.8, 84.1, and 84.2, respectively (Fig. 7). There is a consistent posterior to posterior-lateral inclination within the entire anatomical range (Fig. 8).

Maximum vertical angles exceed those from previous research^{48,60,61}, necessitating manual examination of extreme values. These larger angles may be due to the larger sample size in the current study or from the precision of this method which permits more accurate calculations of osteon vertical angle. High-end osteons that were statistically determined as vertical angle outliers were within two standard deviations of the mean when standardized into z -scores and were manually confirmed to be correct, so were retained. Low-end vertical angle outliers were also identified and retained as previous research found that osteon systems can be inclined at 0°⁶⁰. All octants exhibited high and low outliers when examining osteon horizontal direction. While these may fall outside the general trends per octant, none were excluded as they were within the 360° range.

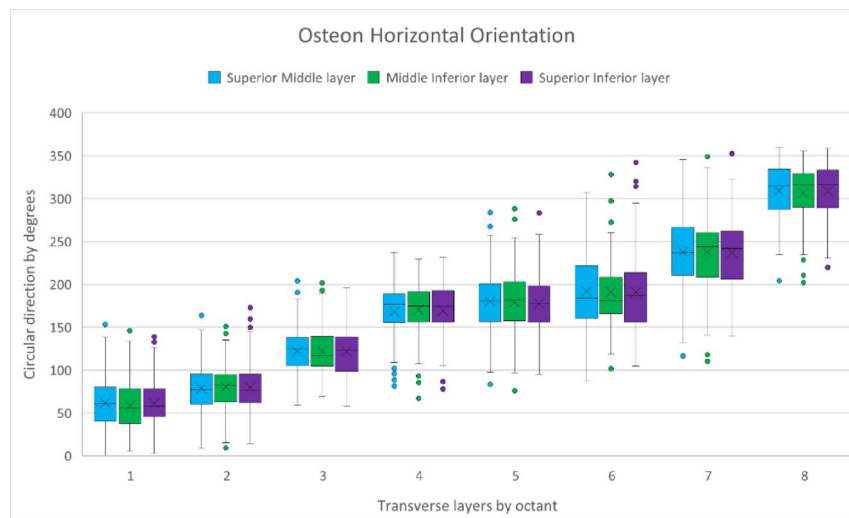


Fig. 7. Box plot showing the mean osteon horizontal direction across the octants, where 0° =oriented anteriorly, 90° =oriented laterally, 180° =oriented posteriorly, and 270° =oriented medially. Blue represents the connected osteons between the superior and middle layers, a distance of approximately $300\ \mu\text{m}$. Green represents the connected osteons between the middle and inferior layers, a distance of approximately $300\ \mu\text{m}$. Purple encompasses the entire viewable osteon between the superior and inferior layers, a distance of approximately $810\ \mu\text{m}$.

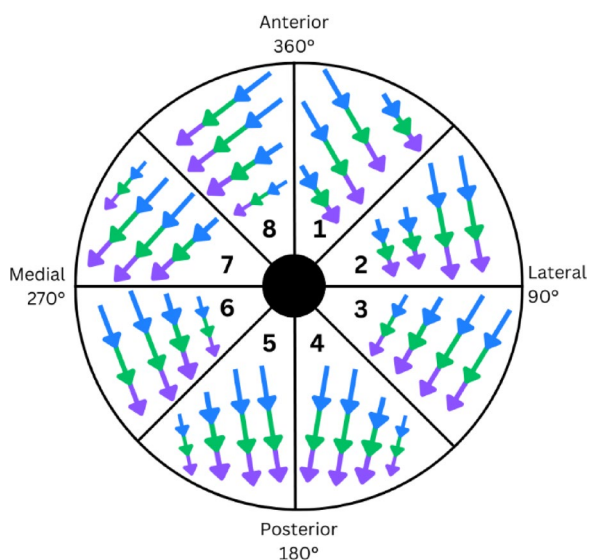


Fig. 8. Average osteon horizontal orientation per octant, revealing that between sections osteons move in a generally posterior direction. Blue arrows represent osteons on the superior transverse section, showing the direction they move towards the green arrows, which represent osteons on the middle transverse section. Green arrows are pointed towards purple arrows, which represent osteons on the inferior transverse section. Osteons in the anterolateral quadrant are oriented towards the posterolateral anatomical plane and those in the anteromedial quadrant are oriented towards the posteromedial. Osteons in the posterolateral quadrant are oriented towards the posteromedial anatomical plane and those in the posteromedial quadrant are oriented towards the posterolateral anatomical plane. The osteons on the medial and lateral halves of the bone are oriented opposite of each other, demonstrating a “helical anti-rotary pattern”⁶⁶ with sharp demarcations at the anterior and posterior sides of the cortex.

Vertical angle descriptives based on octants and circumferential ring

Mean osteon vertical angle varied around the cortex (Table 1) but shows consistency across graded depth. The largest angles were found in the posterior-lateral quadrant (octants 3 & 4) in the SM and MI layers and posteriorly (octants 4 & 6) in the SI layer. The smallest angles were located in the anterior quadrant (octants 1 & 8) in all sets of layers. Osteons present more acute angles in the anterolateral quadrant and a more obtuse angle

in the posterolateral quadrant, with relative consistency along the medial half of the cortex. The average vertical osteon angles were consistent across the three transverse sections when examining the circumferential rings (Table 1). All had the smallest angle in the outer periosteal ring, and the largest angle was found in the inner endosteal ring. Osteon vertical angle is wider closest to the medullary cavity of the bone and narrower at the outer edge of the cortex (Fig. 6).

Horizontal direction descriptives based on octants and circumferential ring

Horizontal direction was also consistent between the three sets of layers (Table 1). Osteons in the anterolateral quadrant were oriented laterally, with a slight posterior inclination. Osteons in octant 3 were directed to the posterior-lateral quadrant. Osteons in octants 4, 5, and 6 were all posteriorly oriented. Osteons in octant 7 were oriented medially, and those in octant 8 were oriented towards the anterior-medial quadrant, while maintaining a slight posterior inclination (Fig. 8). Osteons in the femoral cortex diverge distally from the anterior surface, orienting posteriorly-medially and posteriorly-laterally. They converge near the posterior margin, just lateral to the *linea aspera*. The osteons on the medial and lateral halves are oriented opposite each other, demonstrating what Petrář et al.⁶⁶ described as a “helical anti-rotary pattern” (161) with sharp demarcations at the anterior and posterior cortical surfaces. Horizontal orientation was consistent between the three circumferential rings, indicating no major differences in osteon orientation on the exterior-interior plane.

ANOVA comparisons

ANOVA results indicated within the three samples, each octant was different from all other octants when comparing both osteon vertical angle (SM layer: $F_{7,1211}=16.31$, $p < 0.001$, MI layer: $F_{7,1211}=12.96$, $p < 0.001$, and SI layer: $F_{7,1211}=12.04$, $p < 0.001$) and osteon horizontal direction (SM layer: $F_{7,1211}=925.26$, $p < 0.001$, MI layer: $F_{7,1211}=991.15$, $p < 0.001$, and SI layer: $F_{7,1211}=957.08$, $p < 0.001$). ANOVA results revealed that osteon vertical angle also differed between each circumferential ring (periosteal ring: $F_{2,1216}=21.21$, $p < 0.001$, mid-cortical ring: $F_{2,1216}=15.69$, $p < 0.001$, and endosteal ring: $F_{2,1216}=12.10$, $p < 0.001$). Differences were not seen when comparing osteon horizontal direction between the circumferential rings (periosteal ring: $F_{2,1216}=0.124$, $p = 0.88$, mid-cortical ring: $F_{2,1216}=0.41$, $p = 0.66$, and endosteal ring: $F_{2,1216}=0.414$, $p = 0.66$), likely because these sampling locations comprise osteons from all octants of the cortex. These analyses demonstrate that osteon tilt exhibits regional variation around the cortex.

ANOVA comparisons based on octants

Tukey’s HSD Post-hoc tests quantified the differences seen between the octants and circumferential rings (Supplementary Materials Table 1) for both vertical osteon angle and horizontal osteon direction. Vertical osteon angle in octant 1 is significantly different from octants 2 through 6 but is similar to osteons in octants 7 and 8. Octants 7 and 8 exhibit no significant difference, showing a strong tendency for osteons to be acutely angled in the anterior cortex. However, octant 7, situated anterior-medially, does not significantly differ from octant 6, which it borders, nor from octants 3 and 5 in the SI layer. Octant 7 is not significantly different than octant 2, but octant 8 is, demonstrating that although osteon angle tends to be more acute in the anterior portion of the bone, there remains regional variation between octants. Octants that border each other are often similar; only neighboring octants 1 and 2, and octants 6 and 7, show significant differences between vertical osteon angle, and the latter weakly. In general, all three sets of layers are consistent with each other regardless of whether differences between octants are significant, and vary based on the strength of this difference, indicating that gradations of depth have minimal impact on osteon tilt calculations. However, when examining the longer distance of the SI layer, as compared to the shorter distance of the two other pairs of layers, a few discrepancies emerge. Octant pairs 2 and 4, 3 and 7, and 6 and 7 are not significantly different, whereas they are when looking at the SM and MI layers.

When comparing osteon horizontal direction, almost all octants are significantly different from all other octants. Octants in the posterior half of the cortex do not show significant differences; octant 4 is similar to octant 5, and octant 5 is similar to octant 6. This regional consistency in osteon direction represents the general posterior-lateral inclination seen in the mean of all osteons. These octants are similarly oriented posteriorly. Osteons in the lateral octants are oriented more laterally and posterior-laterally, and those in the medial octants are oriented more medially and posterior-medially. The horizontal direction of osteons in the anterior octants (1 and 8) is significantly different because they mirror each other and are oriented in opposite directions. No octant differences were seen when comparing the three pairs of layers.

ANOVA comparisons based on circumferential rings

When comparing the osteons within the circumferential rings, ANOVA results indicated differences between osteon vertical angle (SM layer: $F_{2,1216}=21.21$, $p < 0.001$, MI layer: $F_{2,1216}=15.69$, $p < 0.001$, and SI layer: $F_{2,1216}=12.10$, $p < 0.001$) but not osteon horizontal direction (SM layer: $F_{2,1216}=0.12$, $p = 0.883$, MI layer: $F_{2,1216}=0.41$, $p = 0.664$, and SI layer: $F_{2,1216}=0.41$, $p = 0.661$). Post-hoc tests revealed that when examining osteon angle, the endosteal ring was significantly different to both the periosteal and mid-cortical rings for all three pairs of layers, but when comparing the periosteal to the mid-cortical rings, only the MI layer was significantly different. There is relative consistency in vertical osteon angle in the outer two circumferential thirds of the bone, and a significant difference to the inner endosteal third, which is closest to the medullary cavity.

Paired sample t-test comparison between layers

A paired sample t-test compared the SM and MI layers. They were not compared to the SI layer, because this layer is comprised of the other two, so the observations would not be independent of each other. Osteon vertical

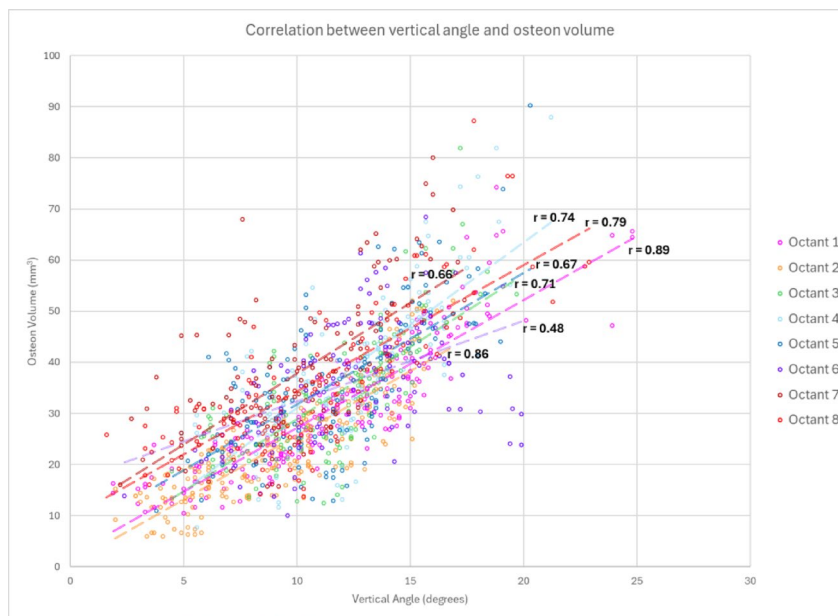


Fig. 9. Scatterplot with trendlines showing the relationship between osteon vertical angle (degrees) and osteon volume (mm^3), with associated correlation coefficient (r), per octant.

angle is strongly and positively correlated between the SM and MI layers ($r=0.91$, $p<0.001$), as is osteon horizontal direction ($r=0.97$, $p<0.001$). There were no significant average differences between either vertical angle ($t_{1218}=0.75$, $p=0.227$) or horizontal direction ($t_{1218}=0.62$, $p=0.538$). The strong correlation and a lack of significant differences in the paired sample t-test demonstrates the effectiveness of the GIS-based volumetric method at maintaining alignment between connected osteons across re-registered serial transverse sections.

Correlation between osteon volume and osteon vertical angle

Correlations were performed to explore the relationship between osteon vertical angle and osteon volume (Fig. 9). The complete osteon (SI layer) was analyzed. In all octants, a positive correlation between the two variables was seen, so a smaller osteon volume is correlated with a narrower angle, and a larger osteon volume coincides with a wider angle. Octants 1 ($r=0.89$, 95% CI [0.86, 0.92]), 2 ($r=0.86$, 95% CI [0.82, 0.89]), and 8 ($r=0.79$, 95% CI [0.71, 0.85]) had the strongest correlations, indicating this relationship is strongest in the anterior portion of the cortex. Octants 3 ($r=0.71$, 95% CI [0.62, 0.79]) and 4 ($r=0.74$, 95% CI [0.65, 0.81]) in the lateral portion of the cortex also had a strong correlation. Octants 5 ($r=0.66$, 95% CI [0.56, 0.75]), 6 ($r=0.48$, 95% CI [0.33, 0.60]), and 7 ($r=0.66$, 95% CI [0.56, 0.75]) on the medial portion of the cortex maintained this positive relationship, but was weaker, demonstrating that there is a strong regional effect to the relationship between osteon vertical angle and osteon volume.

Discussion

The objective of this research study was to visualize and quantify the spatial patterning of osteon tilt around the femoral cortex. This was achieved by combining a GIS-based method with traditional histological serial sectioning. Through analysis of 1219 osteons this study demonstrated that the novel GIS-based method enables a three-dimensional analysis of the relatively unexplored variables of osteon tilt, and that osteon tilt exhibits regional cortical variation. Further insight into this spatial patterning may yield implications for pathology, clinical practice, and forensic science, and the novel GIS-based method could be used for further study in these fields.

GIS-based method validation

The GIS-based method¹⁴ was successfully adapted to explore osteon tilt across cortical regions and serial transverse sections. Comparisons between the two shorter layers (SM and MI, $\sim 300 \mu\text{m}$ depth) with the longer layer (SI, $\sim 810 \mu\text{m}$ depth) showed no substantive differences in osteon tilt variables. Paired sample t-tests confirmed consistency between layers, demonstrating that the method maintains alignment between connected osteons across serial transverse sections, a known shortcoming of traditional serial section histology. This demonstrates accurate re-registration of serial sections for three-dimensional osteon exploration across the entire cortex.

Osteon tilt results align with previous studies, validating the method's applicability. Most studies exploring osteon orientation revealed two spiral systems of opposite oblique directions, separated by a distinct medial-lateral boundary^{48,58,60,64,65}, as seen in this study. However, some previous research did not identify an oblique osteon orientation^{47,49,59,66}. Inconsistencies may reflect differences in sampling strategy, species selection, individual variation, visualization methods, and the limited research in this area. For example, Stout et al.⁹²

used computer-assisted reconstruction of Tappen's⁴⁹ original samples to support Tappen's conclusion that osteons show complex branching rather than spiral organization. However, those sections lacked fixed points of reference for accurate serial section re-registration, potentially compromising topographical relationships. Additionally, only a small cortical portion was studied. The current GIS protocol overcomes these limitations by spatially re-associating multiple disconnected but continuous transverse serial sections using buffers, overlays, joins, and nearest neighbor analysis to provide data on osteon area, distance between osteons, osteon angle, and osteon orientation.

While the osteon orientation results align with previous research, osteon vertical angle results exhibit minor differences. Some angles exceeded the maximum reported in earlier studies⁶⁰, possibly due to differences in sample size, sampling method, or angle visualization and calculation techniques. For example, Cohen and Harris⁴⁸ followed eight grouped osteons in each dog femur sample; conversely, this study followed over 1200. Skedros et al.⁹³ noted different osteon orientation patterns in other quadrupeds (sheep and deer) when compared to humans suggesting locomotory differences may also affect osteon angle, limiting direct comparison between animal and human studies. Heřt et al.'s⁶⁰ maximum average osteon angle of 15° in the human femur used superficial vascular canal staining, so included fragmentary osteons and pores in the calculations, preventing individual osteon angle calculation. Only periosteal canals were examined, whereas this study analyzed superficial and deep osteons, and found larger angles at all depths but greater average angles in the endosteal circumferential ring. Previous research reported regional averages rather than individual osteon ranges; osteons with greater vertical angles may have been encountered but minimally impacted mean values. The present study analyzed osteon tilt data across 24 cortical regions. The only previous regional study⁶⁰ reported mean vertical angles of 8.1° on the lateral half and 10.3° on the medial half. While angles in this study were slightly greater than Heřt et al.'s⁶⁰ findings, a similar relationship emerged with greater angles on the medial half compared to the lateral half. This study additionally found greater angles in the posterior half compared to the anterior half. Lastly, this investigation uniquely employed computerized, GIS-based calculations for precise osteon tilt measurements. Despite occasional extreme values, mean vertical angle aligned with the limited previous research, validating this method for three-dimensional osteon analysis. Consistency between studies, despite methodological differences, suggests these patterns reflect true cortical spatial variation in osteon tilt.

Spatial variation in osteon tilt

Osteon tilt measurements exhibit regional cortical variability. The smallest vertical angles occur in the anterolateral region, while the greatest vertical angles are found in the posterior cortex. The lateral half of the bone shows greater variability compared to the relatively consistent medial half. Vertical angles are smaller in the outer periosteal circumferential ring and larger in the inner endosteal ring. Osteons are oriented contralaterally on the medial and lateral halves with a demarcation at the anterior and posterior surfaces. Osteons on the lateral portion orient laterally and posteriorly, while those on the medial half orient medially and posteriorly, exhibiting a general posterior inclination. No differences in osteon orientation occur circumferentially, likely because the rings average the osteon directions. A positive correlation was also observed between osteon vertical angle and osteon volume: larger osteon volumes coincide with greater vertical angles. The anterolateral region shows the most acute vertical angles and the smallest average osteon volumes, while larger osteons with greater angles are found posteriorly. This consistent regional spatial patterning suggests systematic underlying mechanisms rather than random variation.

Most studies exploring osteon orientation have revealed spatial patterns that align with the present findings^{48,58,60,64,65}, and those that examined osteon angle calculated similar values^{48,51,58,60,61}. Studies that explored other osteon variables have attributed the distinct regional patterns in osteon size^{50,52}, circularity⁵⁰, population density^{53,54}, canal diameter⁵³, morphotype⁹⁴, and collagen fibril orientation^{55–57} to biomechanical influences.

Biomechanical loading of the femoral diaphysis exhibits high-load complexity with overlapping tension and axial compression forces and diffuse shear strains^{55,91,95,96}. Despite this complexity, distinct regional loading patterns exist: the anterolateral quadrant experiences predominately tensile stresses⁹⁷, while the posterior and medial regions experience stronger compressive forces⁹⁷. Although compressed bone tissue experiences 1.9 times greater strain than tensed regions⁹⁸, the human femur is weaker under tension and experiences greater fatigue and microcrack propagation⁹⁹. Targeted bone remodeling initiated by biomechanical forces to repair microdamage may occur at a greater rate in tensed regions^{54,100,101}. The femur also experiences posteriorly directed forces during locomotion, which create femoral bending moments through center of mass and gravitational forces¹⁰².

The spatial osteon patterns may reflect biomechanical adaptations, as bone remodeling responds to mechanical forces through osteocyte-mediated mechanotransduction^{18–20,34–37,69}. Several observations support potential loading-related influences, though further investigation with larger sample sizes is needed to establish definitive connections. The anterolateral region's acute vertical angles and smallest osteon volumes coincide with tensile loading and higher remodeling rates, as evinced by the greater osteon population density observed in this region⁵⁴. Densely packed osteons may be constrained during formation by nearby cutting cones and complete secondary osteons, limiting both angular development and volumetric growth. These smaller, more numerous osteons found in tensile load-bearing regions⁹⁷ may distribute mechanical loads across a broader area, minimizing localized microcrack propagation and increasing bone flexibility. The endosteal circumferential ring's greater vertical angles differ from patterns seen in high-remodeling octant regions, suggesting that endosteal bone turnover may be influenced by factors beyond mechanical strain, such as proximity to the marrow cavity and blood supply¹⁰³. The general posterior osteon orientation may relate to the dominant posteriorly directed locomotory forces¹⁰². Posterior osteon alignment may dissipate bending forces, reducing microcrack propagation and contributing to femoral shaft stability^{102,104}. Larger osteons in the posterior region may be structurally adapted to resist deformation from compressive forces by providing a more solid structure⁹⁷.

Ultimately, the regional spatial variability of osteon tilt, and the correlation between angle and volume, suggest that these morphological features are connected and may collectively respond to the bone's mechanical environment, though the specific mechanisms require further investigation.

Conclusion

Minimal literature on osteon tilt exists due to the technical limitations of visualizing and quantifying this variable. This study successfully combined traditional histology with a customized GIS protocol to create a robust 2.5D method for analyzing osteon tilt across the entire cortex. The new method permits large-scale visualization, quantification, and analysis of bone microarchitecture on multiple planes, exceeding traditional histological sectioning and surpassing the field of view of micro- or nano-CT imaging techniques^{5,6,70,73}. This enhanced understanding of osteon formation, development, regional patterns, and interrelationships provides new insights into these histological structures and may help address questions regarding biomechanical influences on bone remodeling.

Biomechanical inputs may impact osteon tilt^{48,53,60,65,67}. Previous literature suggests that osteon structure optimizes bone's resistance to fatigue and failure^{20,31,54,105}. The findings demonstrate that osteon tilt in the femoral midshaft is not random, with acute angles seen in the anterolateral region and obtuse angles posteriorly. This patterning, combined with the positive correlation between osteon angle and volume, suggests that osteon orientation and morphology may represent adaptive responses to local mechanical environments. The cortical variation of osteon angle and the general posterior osteon orientation may reflect localized adaptations to different loading conditions. Since other microstructural elements also vary in tensed and compressed regions^{1,14,52,54,55,100,101}, osteon tilt may provide a reliable characteristic for understanding loading history complexity, complementing established methods using collagen fiber orientation and osteon morphotype distribution^{53,55,106}. Three-dimensional osteon exploration may offer insights into femoral loading mechanisms that traditional two-dimensional variables, such as osteon area, osteon population density, or cross-sectional size^{54,107–109}, have not provided.

This study is the first to comprehensively analyze osteon tilt across the femoral cortex, providing future applications to bone biology, histology, pathology, and forensic anthropology. Continued development of the GIS-based method will enhance understanding of microarchitectural variability and factors influencing osteon development. Future incorporation of artificial intelligence models and machine learning and deep learning^{70,110} could expedite analysis and expand the method's utility.

Data availability

The datasets generated and analysed during the current study are available from the corresponding author upon reasonable request.

Received: 10 May 2025; Accepted: 20 October 2025

Published online: 21 November 2025

References

- Báča, V., Kachlík, D., Horák, Z. & Stingl, J. The course of osteons in the compact bone of the human proximal femur with clinical and biomechanical significance. *Surg. Radiol. Anat.* **29**, 201–207 (2007).
- Cowin, S. C. *Bone Mechanics Handbook* (CRC, 2001).
- Wallace, J. M. Skeletal Hard Tissue Biomechanics in *Basic and applied bone biology* (eds Burr, D. & Allen, A.) 115–130 (Academic Press, 2014).
- Martin, R. B. & Burr, D. B. *Skeletal Tissue Mechanics* 2nd edn (Springer, 2015).
- Andronowski, J. M. & Cole, M. E. Current and emerging histomorphometric and imaging techniques for assessing age-at-death and cortical bone quality. *WIREs Forensic Sci.* **3**, 3e1399. <https://doi.org/10.1002/wfs2.1399> (2021).
- Harrison, K. D. & Cooper, D. M. L. Modalities for visualization of cortical bone remodeling: the past, present, and future. *Front. Endocrinol. (Lausanne)*. **6**. <https://doi.org/10.3389/fendo.2015.00122> (2015).
- Akhter, M. P. & Recker, R. R. High resolution imaging in bone tissue research. *Bone* **142**, 115620. <https://doi.org/10.1016/j.bone.2020.115620> (2021).
- Hennig, C., Thomas, C., Clement, J. & Cooper, D. Does 3D orientation account for variation in osteon morphology assessed by 2D histology? *J. Anat.* **227**, 497–505 (2015).
- Doube, M. Closing cones create conical lamellae in secondary osteonal bone. *R Soc. Open. Sci.* **9**, 220712. <https://doi.org/10.1098/rsos.220712> (2022).
- Ford, N. L., Thornton, M. M. & Holdsworth, D. W. Fundamental image quality limits for microcomputed tomography in small animals. *Med. Phys.* **30**, 2869–2877 (2003).
- Rose, D., Agnew, A., Gocha, T., Stout, S. & Field, J. Technical note: the use of geographical information systems software for the spatial analysis of bone microstructure. *Am. J. Phys. Anthropol.* **148**, 648–654 (2012).
- Garb, J. L. Mapping the human body: A GIS perspective in Mapping across Academia (eds Brunn, S. D. & Dodge, M.) 105–122 (Springer, 2017).
- Mallouchou, M. et al. Mapping Cheshire cats' leg: A histological approach of cortical bone tissue through modern GIS technology. *Anat. Sci. Int.* **95**, 104–125 (2020).
- Michener, S., Bell, L. S., Schuurman, N. C. & Swanlund, D. A method to interpolate osteon volume designed for histological age Estimation research. *J. Forensic Sci.* **65**, 1247–1259 (2020).
- Dalle Carbonare, L. et al. Bone microarchitecture evaluated by histomorphometry. *Micron* **36**, 609–616 (2005).
- Ruff, C. Biomechanical analyses of archaeological human skeletons in Biological Anthropology of the Human Skeleton (eds Katzenberg, A. & Saunders) 183–206 (John Wiley & Sons, Inc., 2008).
- Ravazzano, L. et al. Multiscale and multidisciplinary analysis of aging processes in bone. *Npj Aging*. **10**, 28. <https://doi.org/10.1038/s41514-024-00156-2> (2024).
- Burr, D. Targeted and nontargeted remodeling. *Bone* **30**, 2–4 (2002).
- Martin, R. B. Is all cortical bone remodeling initiated by microdamage? *Bone* **30**, 8–13 (2002).
- Allen, M. & Burr, D. Bone modeling and remodelling in Basic and Applied Bone Biology (eds Burr, D. & Allen, A.) 75–90 (Academic, 2014).

21. Jee, S. CRC Press, Integrated bone tissue physiology: anatomy and physiology in *Bone mechanics handbook* (ed. Cowin, S) 1-1-1-68 (2001).
22. Chen, H., Zhou, X., Fujita, H., Onozuka, M. & Kubo, K.-Y. Age-Related changes in trabecular and cortical bone microstructure. *Int. J. Endocrinol.* **213234** <https://doi.org/10.1155/2013/213234> (2013).
23. Kenkre, J. S. & Bassett, J. H. D. The bone remodelling cycle. *Ann. Clin. Biochem.* **55**, 308–327 (2018).
24. Robling, A. & Bonewald, L. F. The osteocyte: new insights. *Annu. Rev. Physiol.* **82**, 495–506 (2020). (2020).
25. Hadjidakis, D. J. & Androulakis, I. I. Bone remodeling. *Ann. N Y Acad. Sci.* **1092**, 385–396 (2006).
26. Raggat, L. J. & Partridge, C. P. Cellular and molecular mechanisms of bone remodeling. *J. Biol. Chem.* **285**, 25103–25108 (2010).
27. Cole, M. E., Crowder, C. & Stout, S. D. Bone remodeling and its histomorphological products in *Bone histology: A biological anthropological perspective, 2nd edition* (eds Stout, S. D. & Crowder, C.) 1–46CRC Press, (2025).
28. Eriksen, E. F. Cellular mechanisms of bone remodeling. *Rev. Endocr. Metab.* **11**, 219–227 (2010).
29. Robling, A., Fuchs, R. & Burr, D. Mechanical adaptation in Basic and Applied Bone Biology (eds Burr, D. & Allen, A.) 175–204 (Academic, (2014).
30. Wolff, J. *The Law of Bone Transformation (in German, trans. Maquet 1892* (Springer-, 1986). Furlong, R.
31. Frost, H. The regional acceleratory phenomenon: a review. *Henry Ford Hosp. Med. Bull.* **31**, 3–9 (1983).
32. Cowin, S. C. Wolff's law of trabecular architecture at remodeling equilibrium. *J. Biomech. Eng.* **108**, 83–88 (1986).
33. Turner, C. H. On Wolff's law of trabecular architecture. *J. Biomech.* **25**, 1–9 (1992).
34. Nareliya, R. & Kumar, V. Biomechanical analysis of human femur bone. *Int. J. Eng. Sci. Technol.* **3**, 3090–3094 (2011).
35. Burr, D. B. & Akkus, O. Bone morphology and function in Basic and Applied Bone Biology (eds Burr, D. & Allen, A.) 24–45 (Academic, (2014).
36. Bonewald, L. F. Osteocytes as orchestrators of bone adaptation to load. *Ann. N Y Acad. Sci.* **1116**, 281–290 (2007).
37. Cowin, S. The significance of bone microstructure in mechanotransduction. *J. Biomech.* **40**, S105–S109 (2007).
38. Turner, C. Toward a mathematical description of bone biology: the principle of cellular accommodation. *Calcif Tissue Int.* **65**, 466–471 (1999).
39. Turner, C. H. Toward a mathematical description of bone biology: the principle of cellular accommodation. *Calcif Tissue Int.* **67**, 185–187 (2000).
40. Bonewald, L. F. The amazing osteocyte. *J. Bone Min. Res.* **26**, 229–238 (2011).
41. Robling, A. G. & Turner, C. H. Mechanical signaling for bone modeling and remodeling. *Crit. Rev. Eukaryot. Gene Expr.* **19**, 319–338 (2009).
42. Christen, P. et al. Bone remodelling in humans is load-driven but not lazy. *Nat. Commun.* **5**, 4855. <https://doi.org/10.1038/ncomms5855> (2014).
43. Bellido, T., Plotkin, L., Bruzzaniti, A. & Bone cells in *Basic and applied bone biology* (eds Burr, D. & Allen, A.) 3–26Academic Press, (2014).
44. Ross, F. P. Osteoclast biology and bone resorption in *Primer on the Metabolic Bone Diseases and Disorders of Mineral Metabolism* (eds Rosen, C. J. et al.) 25–33 (John Wiley & Sons, Inc., (2013).
45. Maggiano, I. S., Maggiano, C. M. & Cooper, D. M. L. Osteon circularity and longitudinal morphology: quantitative and qualitative three-dimensional perspectives on human Haversian systems. *Micron* **140**, 102955. <https://doi.org/10.1016/j.micron.2020.102955> (2021).
46. Cooper, D., Thomas, C., Clement, J. & Hallgrímsson, B. Three-dimensional microcomputed tomography imaging of basic multicellular unit-related resorption spaces in human cortical bone. *Anat. Rec Part. A.* **288A**, 806–816 (2006).
47. Koltze, H. Study on the external shape of osteons (in German). *Zeitschr F Anat. Entw.* **115**, 584–591 (1951). (1951).
48. Cohen, J. & Harris, W. H. The three-dimensional anatomy of Haversian systems. *J. Bone Joint Surg.* **40A**, 419–434 (1958).
49. Tappen, N. C. Three-dimensional studies on resorption spaces and developing osteons. *Am. J. Anat.* **149**, 301–317 (1977).
50. Britz, H., Thomas, C., Clement, J. & Cooper, D. The relation of femoral osteon geometry to age, sex, height and weight. *Bone* **45**, 73–83 (2009).
51. Maggiano, I. S. et al. Three-dimensional reconstruction of Haversian systems in human cortical bone using synchrotron radiation-based micro-CT: morphology and quantification of branching and transverse connections across age. *J. Anat.* **228**, 719–732 (2016).
52. van Oers, R. F., Ruimerman, R., van Rietbergen, B., Hilbers, P. A. & Huiskes, R. Relating osteon diameter to strain. *Bone* **43**, 476–482 (2008).
53. Skedros, J. G., Keenan, K. E., Williams, T. J. & Kiser, C. J. Secondary osteon size and collagen/lamellar organization ('osteon morphotypes') are not coupled, but potentially adapt independently for local strain mode or magnitude. *J. Struct. Biol.* **181**, 95–107 (2013).
54. Gocha, T. & Agnew, A. Spatial variation in osteon population density at the human femoral midshaft: histomorphometric adaptations to habitual load environment. *J. Anat.* **228**, 733–745 (2015).
55. Skedros, J. G. Biomechanical foundations of histological analysis in limb bones: The crucial role of load-complexity categorization and collagen fiber orientation analysis when interpreting bone adaptation in *Bone histology: A biological anthropological perspective, 2nd edition* (eds Stout, S. D. & Crowder, C.) 150–224CRC Press, (2025).
56. Reznikov, N., Chase, H., Brumfeld, V., Shahar, R. & Weiner, S. The 3D structure of the collagen fibril network in human trabecular bone: relation to trabecular organization. *Bone* **71**, 189–195 (2015).
57. Georgiadis, M., Müller, R. & Schneider, P. Techniques to assess bone ultrastructure organization: orientation and arrangement of mineralized collagen fibrils. *J. R Soc. Interface.* **13**, 119. <https://doi.org/10.1098/rsif.2016.0088> (2016).
58. Martin, R. B. & Burr, D. B. *Structure, Function and Adaptation of Compact Bone* (Raven, 1989).
59. Schumacher, S. On the arrangement of the vascular canals in the diaphysis of long bones in humans (in German). *Z. Zellf Mikr Anat.* **38**, 145–160 (1935).
60. Heřt, J., Fiala, P. & Petrýl, P. Osteon orientation of the diaphysis of the long bones in man. *Bone* **15**, 269–277 (1994).
61. Lanyon, L. E. & Bourn, S. The influence of mechanical function on the development and remodeling of the tibia. An experimental study in sheep. *J. Bone Joint Surg.* **61A**, 263–273 (1979).
62. Martínez-Reina, J., Reina, I., Domínguez, J. & García-Aznar, J. M. A bone remodelling model including the effect of damage on the steering of BMUs. *J. Mech. Behav. Biomed. Mater.* **32**, 99–112 (2014).
63. Burger, E. H., Klein-Nulend, J. & Smit, T. H. Strain-derived canalicular fluid flow regulates osteoclast activity in a remodelling osteon—a proposal. *J. Biomech.* **36**, 1453–1459 (2003).
64. Sinel'nikov, N. A. Spatial architecture of osteons in the diaphysis of the femur in man and other primates (in Russian). *Anthrop Zurnal.* **3**, 102–115 (1937).
65. Petrýl, M., Heřt, J. & Fiala, P. Spatial organization of the Haversian bone in man. *J. Biomech.* **29**, 161–169 (1996). (1996).
66. Benninghoff, A. Cleavage lines on bone, a method for determining the architecture of flat bones (in German). *Verh Anat. Ges.* **34**, 189–206 (1925).
67. Skedros, J. G., Hunt, K. J. & Bloebaum, R. D. Relationships of loading history and structural and material characteristics of bone: development of the mule deer calcaneus. *J. Morphol.* **259**, 281–307 (2004).
68. Buss, D. J., Kröger, R., McKee, M. D. & Reznikov, N. Hierarchical organization of bone in three dimensions: A twist of twist. *J. Struct. Biol.* **100057** <https://doi.org/10.1016/j.jsbx.2021.100057> (2022).

69. Ganesh, T., Laughrey, L. E., Niroobakhsh, M. & Lara-Castillo, N. Multiscale finite element modeling of mechanical strains and fluid flow in osteocyte lacunocanalicular system. *Bone* **137**, 115328. <https://doi.org/10.1016/j.bone.2020.115328> (2020).
70. Cooper, D., Andronowski, J. M., Wei, X. & Taylor, J. T. Three-dimensional microstructural imaging of bone: Technological developments and anthropological applications in *Bone histology: A biological anthropological perspective, 2nd edition* (eds: Stout, S. D. & Crowder, C.) 393–441 CRC Press, (2025).
71. Andronowski, J. M., Pratt, I. V. & Cooper, C. M. L. Occurrence of osteon banding in adult human cortical bone. *Am. J. Phys. Anthropol.* **164**, 635–642 (2017).
72. Manske, S. L., Davison, E. M., Burt, L. A., Raymond, D. A. & Boyd, S. K. The Estimation of second-generation HR-pQCT from first-generation HR-pQCT using in vivo cross-calibration. *J. Bone Min. Res.* **32**, 1514–1524 (2017).
73. Ayoubi, M. et al. 3D interrelationship between osteocyte network and forming mineral during human bone remodeling. *Adv. Healthc. Mater.* **10**, 2100113. <https://doi.org/10.1002/adhm.202100113> (2021).
74. Waters, N. Tobler's first law of geography in The International Encyclopedia of Geography. (eds: (eds Richardson, D., Castree, N., Goodchild, M. F., Kobayashi, A., Liu, W. & Marston, R. A.) DOI: <https://doi.org/10.1002/9781118786352.wbieg1011> (John Wiley & Sons, Ltd., (2017).
75. ESRI. 3D GIS terminology [https://](https://pro.arcgis.com/en/pro-app/latest/help/analysis/3d-analyst/essential-3d-analyst-terms.htm) (2025). pro.arcgis.com/en/pro-app/latest/help/analysis/3d-analyst/essential-3d-analyst-terms.htm
76. Longley, P. A., Goodchild, M. F., Maguire, D. J. & Rhind, D. W. *Geographical Information Systems and Science, 2nd ed.* (John Wiley & Sons, (2005).
77. Khan, S. & Aaqid, S. M. Empirical evaluation of ArcGIS with contemporary open source solutions - A study. *Int. J. Adv. Res. Sci. Eng. Technol.* **6**, 724–736 (2017).
78. Gocha, T. P., Mavroudas, S. R. & Goldstein, J. Z. CRC Press., Age-at-death estimation from bone microstructure in *Bone histology: A biological anthropological perspective, 2nd edition* (eds: Stout, S. D. & Crowder, C.) 270–306 (2025).
79. Garb, J. L., Ganai, S., Skinner, R., Boyd, C. S. & Wait, R. B. Using GIS for Spatial analysis of rectal lesions in the human body. *Int. J. Health Geogr.* **6**, 1–14 (2007).
80. Roth, N. M. & Kiani, M. F. A geographic information systems based technique for the study of microvascular networks. *AMBE* **27**, 42–47 (1999).
81. Knothe Tate, M. L. et al. Organ-to-cell-scale health assessment using geographic information system approaches with multibeam scanning electron microscopy. *Adv. Healthc. Mater.* **5**, 1581–1587 (2016).
82. Cambra-Moo, O. et al. Mapping human long bone compartmentalisation during ontogeny: A new methodological approach. *J. Struct. Biol.* **178**, 338–349 (2012).
83. Crowder, C., Dominguez, V. M., Heinrich, J., Pinto, D. & Mavroudas, S. Analysis of histomorphometric variables: proposal and validation of osteon definitions. *J. Forensic Sci.* **67**, 80–91 (2022).
84. Wade, T. & Sommer, S. *A To Z GIS* (ESRI, 2006).
85. Tobler, W. R. A computer movie simulating urban growth in the Detroit region. *Econ. Geogr.* **46**, 234–270 (1970).
86. ESRI. An overview of the Proximity toolset [https://](https://pro.arcgis.com/en/pro-app/latest/tool-reference/analysis/an-overview-of-the-proximity-toolset.htm) (2025). pro.arcgis.com/en/pro-app/latest/tool-reference/analysis/an-overview-of-the-proximity-toolset.htm
87. ESRI. Generate near table (Analysis) (2025). <https://pro.arcgis.com/en/pro-app/latest/tool-reference/analysis/generate-near-table.htm>
88. Skedros, J. G., Sorenson, S. M. & Jenson, N. H. Are distributions of secondary osteon variants useful for interpreting load history in mammalian bones? *Cells Tissues Organs.* **185**, 285–307 (2007).
89. Ascenzi, A. & Bonucci, E. The compressive properties of single osteons. *Anat. Rec.* **161**, 377–392 (1968a).
90. Ascenzi, A. & Bonucci, E. The tensile properties of single osteons. *Anat. Rec.* **158**, 375–386 (1967).
91. Goldman, H. M., Bromage, T. G., Thomas, C. D. L. & Clement, J. G. Preferred collagen fiber orientation in the human mid-shaft femur. *Anat. Rec Part. A.* **272A**, 434–445 (2003).
92. Stout, S. D. et al. Computer-assisted 3D reconstruction of serial sections of cortical bone to determine the 3D structure of osteons. *Calcif Tissue Int.* **65**, 280–284 (1999).
93. Skedros, J. G., Mason, M. W. & Bloebaum, R. D. Differences in osteonal micromorphology between tensile and compressive cortices of a bending skeletal system: indications of potential strain-specific differences in bone microstructure. *Anat. Rec.* **239**, 405–413 (1994).
94. Skedros, J. G. & Doutré, M. S. Collagen fiber orientation pattern, osteon morphology and distribution, and presence of laminar histology do not distinguish torsion from bending in Bat and pigeon wing bones. *J. Anat.* **23**, 748–763 (2019).
95. Duda, G. N. et al. Influence of muscle forces on femoral strain distribution. *J. Biomech.* **31**, 841–846 (1998).
96. Lieberman, D. E., Polk, J. D. & Demes, B. Predicting long bone loading from cross-sectional geometry. *Am. J. Phys. Anthropol.* **123**, 156–171 (2004).
97. Rudman, K., Aspden, R. & Meakin, J. Compression or tension? The stress distribution in the proximal femur. *BioMed. Eng. OnLine.* **5**, 12. <https://doi.org/10.1186/1475-925X-5-12> (2006).
98. Lanyon, L. E. & Baggott, D. G. Mechanical function as an influence on the structure and form of bone. *J. Bone Joint Surg. Br.* **58-B**, 436–443 (1976).
99. George, W. T. & Vashishth, D. Damage mechanisms and failure modes of cortical bone under components of physiological loading. *J. Orthop. Res.* **23**, 1047–1053 (2005).
100. Portigliatti Barbos, M., Bianco, P., Ascenzi, A. M., Bianco, P., Ascenzi, A. & Distribution of osteonic and interstitial components in the human femoral shaft with reference to structure, calcification and mechanical properties. *Acta Anat.* **115**, 178–186 (1983).
101. Goldman, H. M., Thomas, C. D. L., Clement, J. G. & Bromage, T. G. Relationships among microstructural properties of bone at the human midshaft femur. *J. Anat.* **206**, 127–139 (2005).
102. Kennedy, E. A. et al. Lateral and posterior dynamic bending of the mid-shaft femur: fracture risk curves for the adult population. *Stapp Car Crash J.* **48**, 27–51 (2004).
103. Martin, B. Aging and strength of bone as a structural material. *Calcif Tissue Int.* **53**, S39–S40 (1993).
104. Bhardwaj, A., Gupta, A. & Tse, K. M. Mechanical response of femur bone to bending load using finite element method. *RAECS* <https://doi.org/10.1109/RAECS.2014.6799594> (2014).
105. Stout, S. & Crowder, C. Bone remodeling, histomorphology, and histomorphometry in Bone Histology: an Anthropological Perspective (eds Crowder, C. & Stout, S.) 1–22 (CRC, (2012).
106. Skedros, J. G., Kiser, C. J. & Mendenhall, S. D. A weighted osteon morphotype score outperforms regional osteon percent prevalence calculations for interpreting cortical bone adaptation. *Am. J. Phys. Anthropol.* **144**, 41–50 (2011).
107. Burr, D. B., Ruff, C. B. & Thompson, D. D. Patterns of skeletal histologic change through time: comparison of an archaic native American population with modern populations. *Anat. Rec.* **226**, 307–313 (1990).
108. Pfeiffer, S., Crowder, C., Harrington, L. & Brown, M. Secondary osteons and Haversian Canal dimensions as behavioral indicators. *Am. J. Phys. Anthropol.* **131**, 460–468 (2006).
109. Robling, A. G. & Stout, S. D. Histomorphology, geometry, and mechanical loading in past populations in Bone Loss and Osteoporosis: an Anthropological Perspective (eds Agarwal, S. C. & Stout, S. D.) 189–205 (Kluwer Academic/Plenum, (2003).
110. Reznikov, N., Buss, D. J., Provencher, B., McKee, M. D. & Piché, N. Deep learning for 3D imaging and image analysis of biomineralization research. *J. Struct. Biol.* **212**, 107598. <https://doi.org/10.1016/j.jsb.2020.107598> (2020).

Acknowledgements

Canadian Foundation for Innovation: Number 13194.
BC Knowledge Development Fund: Number 804354.
Social Sciences and Humanities Research Council: Number 435-2023-0651.

Author contributions

S.M. wrote the main manuscript text. Figures created by S.M. and D.S. S.M. and L.S.B. conceived research design, analysed and interpreted results. N.S. and D.S. guided spatial and GIS components. All authors reviewed final manuscript.

Declarations

Competing interests

The authors declare no competing interests.

Ethics approval

Ethics for this project was granted by Simon Fraser University's Office of Research Ethics (study no. 2018s0137).

Additional information

Supplementary Information The online version contains supplementary material available at <https://doi.org/10.1038/s41598-025-25378-6>.

Correspondence and requests for materials should be addressed to S.M.

Reprints and permissions information is available at www.nature.com/reprints.

Publisher's note Springer Nature remains neutral with regard to jurisdictional claims in published maps and institutional affiliations.

Open Access This article is licensed under a Creative Commons Attribution-NonCommercial-NoDerivatives 4.0 International License, which permits any non-commercial use, sharing, distribution and reproduction in any medium or format, as long as you give appropriate credit to the original author(s) and the source, provide a link to the Creative Commons licence, and indicate if you modified the licensed material. You do not have permission under this licence to share adapted material derived from this article or parts of it. The images or other third party material in this article are included in the article's Creative Commons licence, unless indicated otherwise in a credit line to the material. If material is not included in the article's Creative Commons licence and your intended use is not permitted by statutory regulation or exceeds the permitted use, you will need to obtain permission directly from the copyright holder. To view a copy of this licence, visit <http://creativecommons.org/licenses/by-nc-nd/4.0/>.

© The Author(s) 2025